

## Article

# Fabrication of Electrospun Xylan-g-PMMA/TiO<sub>2</sub> Nanofibers and Photocatalytic Degradation of Methylene Blue

Yangyang Xie <sup>1,2,†</sup>, Xiao-Feng Sun <sup>1,2,\*</sup>, Wenbo Li <sup>3,†</sup>, Junhui He <sup>2,†</sup>, Ran Sun <sup>1,2,\*</sup>, Sihai Hu <sup>1,2</sup> and Yaoguo Wu <sup>1,2</sup>

<sup>1</sup> Shenzhen Research Institute, Northwestern Polytechnical University, Shenzhen 518057, China; yangyang636@mail.nwpu.edu.cn (Y.X.); husihai@nwpu.edu.cn (S.H.); wuygal@nwpu.edu.cn (Y.W.)

<sup>2</sup> Research Centre of Advanced Chemical Engineering, School of Chemistry and Chemical Engineering, Northwestern Polytechnical University, Xi'an 710129, China; hjhui@mail.nwpu.edu.cn

<sup>3</sup> Queen Mary University of London Engineering School, Northwestern Polytechnical University, Xi'an 710129, China; liwenbo666@mail.nwpu.edu.cn

\* Correspondence: xf001sn@nwpu.edu.cn (X.-F.S.); sunran@nwpu.edu.cn (R.S.)

† These authors contributed equally to this work.

**Abstract:** Herein, xylan-g-PMMA was synthesized by grafting poly(methyl methacrylate) (PMMA) onto xylan and characterized by FT-IR and HSQC NMR spectroscopies, and the xylan-g-PMMA/TiO<sub>2</sub> solution was used to electrospun nanofibers at the voltage of 15 Kv, which was the first time employing xylan to electrospun nanofibers. Moreover, the electrospinning operating parameters were optimized by assessing the electrospinning process and the morphology of electrospun fibers, as follows: the mixed solvent of DMF and chloroform in a volume ratio of 5:1, an anhydroxylose unit (AXU)/MMA molar ratio lower than 1:2, the flow speed of 0.00565–0.02260 mL/min, and a receiving distance of 10–15 cm. Diameters of the electrospun fibers increased with increasing DMF content in the used solvent mixture, MMA dosage, and receiving distance. TiO<sub>2</sub> nanoparticles were successfully dispersed in electrospun xylan-g-PMMA nanofibers and characterized by scanning electron microscopy, energy dispersive X-ray diffraction spectrum, and X-ray photoelectron spectroscopy, and their application for methylene blue (MB) degradation presented above 80% photocatalytic efficiency, showing the good potential in water treatment.

**Keywords:** xylan; PMMA; electrospinning; TiO<sub>2</sub>; photocatalytic degradation



**Citation:** Xie, Y.; Sun, X.-F.; Li, W.; He, J.; Sun, R.; Hu, S.; Wu, Y. Fabrication of Electrospun Xylan-g-PMMA/TiO<sub>2</sub> Nanofibers and Photocatalytic Degradation of Methylene Blue. *Polymers* **2022**, *14*, 2489. <https://doi.org/10.3390/polym14122489>

Academic Editors: Seongpil An and Alexander Malkin

Received: 16 May 2022

Accepted: 16 June 2022

Published: 18 June 2022

**Publisher's Note:** MDPI stays neutral with regard to jurisdictional claims in published maps and institutional affiliations.



**Copyright:** © 2022 by the authors. Licensee MDPI, Basel, Switzerland. This article is an open access article distributed under the terms and conditions of the Creative Commons Attribution (CC BY) license (<https://creativecommons.org/licenses/by/4.0/>).

## 1. Introduction

Electrospinning, short for electrostatic spinning, is an old fiber fabrication technique, but now it serves as a convenient and facile method for the preparation of multilevel functional nanometer-scale polymer fibers [1,2], which was observed in 1897 by Rayleigh, studied in detail by Zeleny on electro-spraying in 1914 [3], patented by Formhals in 1934 [4], and finally made tremendous progress in theory and practice due to the efforts of Taylor [5]. Electrospinning, an electrohydrodynamic procedure, is typically considered to be the process of liquid droplets being electrified to generate jets, followed by stretching and elongating to yield fibers [6]. In the electrostatic spinning process, the polymer solution or melt forms a jet in a strong electric field, and the droplet at the tip of the needle will transform from a spherical shape to a conical shape, known as a Taylor cone, which will extend from the tip of the cone to produce a fibrous filament. In this way, polymer filaments of nanometer diameter can be obtained [7–9]. Over the past few years, electrostatic spinning has been extensively adopted for the fabrication of various nanofiber materials, out of which the organic polymers in solution or melt form are the most commonly used materials [10]. A wide range of synthetic polymers (polyoxyethylene [11], polylactic acid [12,13], polyacrylonitrile [14], polyamide [15], polycaprolactone [16], polyvinyl pyrrolidone [17], polyvinylidene difluoride [18], polyethersulfone [19]) and natural polymers

(collagen [20], chitosan [21], cellulose [22,23], etc.), or a blend of both [11,24], have been applied in electrospinning to prepare nanofibers, as they are soluble or do not degrade at their melting points [1,15]. Nevertheless, compared to synthetic polymers, natural polymers present advantages such as being biodegradable, safe, non-toxic, excellent biocompatibility, economical, and easily available [10,25–28].

In the aspect of abundant and renewable plant resources, hemicellulose is only less than cellulose in percentage composition and is defined as the group of heteroglycans consisting of xylose, mannose, arabinose, galactose, glucose, and 4-O-methyl-D-glucuronic acid residues, which were not widely applied owing to their complex chemical structure and low molecular weight [29–32]. Xylan hemicellulose is extracted from wheat straw, which is soluble in water and composes 53.58–68.34% of hemicellulose material [33–35]. Prevalent studies showed that xylan is composed of a backbone of  $\beta$ -(1→4)-linked hydroxylase units, where the C-2 and C-3 positions are linked with hydroxyl groups or their derivatives [33,36]. Due to its newly certified surface-active, bioactive, antimicrobial, biocompatible, and oxygen barrier properties [37,38], considerable interest has been focused on xylan in applications of sewage treatment [39], food packaging [40,41], drug delivery [35,42], and tissue engineering [36,43]. In addition, many organic polymers used in electrospinning have been reported in the past, but there are few reports about xylan electrospinning. Therefore, employing xylan to prepare novel nanofiber materials that combine the properties of xylan itself with the advantages of nanofibers by the electrospinning method is a worthy research direction.

Diameters of electrospun fibers range from 100 nm to 1  $\mu$ m, which means electrospun fiber mats provide a huge specific surface area with high porosity. Furthermore, the microscopic fine structure of the electrospun fibers is controllable [44,45]. Due to those advantages, electrospun fibers have potential in catalysis [46,47], filtration membrane [48,49], drug delivery [50,51], photocatalysis [52], antibacterial [53], and other applications [54,55]. In recent years, numerous methods have been reported to increase the specific surface area of catalysts for enhancing the efficiency of catalytic reactions [56,57]. A straightforward method of increasing the surface area is to make the catalyst into a nanometer scale. However, this will cause enormous wastage when those nanometer-scale materials are in use due to their difficulty in separating nanometer-scale catalysts from the remaining raw materials and products. A further improvement is loading the catalysts on a porous and hard substrate, which generally is a kind of adsorbing material, such as glasses or ceramics. However, this would decrease the reactive sites, and those inorganic substrates always have some inevitable surficial defects, and the interaction between the catalyst and the substrate is physical and weak. To minimize these negative effects and to expand the available catalytic material resources, nanoscale organic polymer electrospun fibers can be promising candidates for catalysts or their substrates attributed to their fine microscopic nature, huge specific surface area, high porosity, and convenience in preparation [58,59]. Therefore, compounding nanofibers with catalysts is a promising idea to prepare efficient photocatalysts.

In numerous photocatalysts, titanium dioxide ( $\text{TiO}_2$ ), due to its excellent chemical stability, low cost, non-toxicity, safety, and efficient photocatalytic activity, is used extensively in energy and environmental areas [60–64], such as hydrogen production from decomposing water [65–67], pollutant decomposition in water [68,69], and carbon dioxide reduction [70–72]. The photocatalytic properties of  $\text{TiO}_2$  depend on the crystalline structure, which modifies its bandgap. In fact, there are three polymorphs: anatase, rutile, and brookite [73,74].  $\text{TiO}_2$  is one of the most important photocatalytic materials because it is a wide-bandgap semiconductor material ( $\sim 3.2$  eV) suitable only to absorb UV light, and hence photogenerated charge carriers, electrons in the conduction band, and holes in the valence band [63,64]. The electrons are of high reducibility, which can deoxidize the substance absorbed on the surface of  $\text{TiO}_2$ , while the holes are of high oxidizability, which can oxidize the absorbed substance by capturing its electrons. When it is applied in photocatalytic degradation, the holes of  $\text{TiO}_2$  oxidize the absorbed water on the surface,

producing hydroxide free radicals ( $\bullet\text{OH}$ ), and the electrons of  $\text{TiO}_2$  react with oxygen-producing superoxide free radicals ( $\bullet\text{O}^{2-}$  and  $\bullet\text{OOH}$ ), which can all violently oxidize adsorbed pollution on the surface of  $\text{TiO}_2$  [75–77]. Despite the considerable advances that have been achieved in  $\text{TiO}_2$  in the field of photocatalysis, many problems remain, which presents some attractive challenges. One of the issues that cannot be ignored is that the normal usages of  $\text{TiO}_2$  include powder, coating on the membrane surface, or casting into an alloy block, which all decrease the actual catalytic efficiency of  $\text{TiO}_2$  and are uneconomical for the high cost of separating nanometer-scale catalysts from the remaining raw materials and products. However, loading  $\text{TiO}_2$  on electrospun fibers can solve those problems.

In this study, PMMA was grafted on biopolymer xylan to electrospun nanofibers for the first time. The chemical structural features of the synthesized products were proven by FT-IR and NMR analyses. The factors, including the molar ratio of raw materials, solvent, flow speed, and receiving distance, affected the electrospinning process, and the prepared nanofibers were studied by assessing the operability of the process and the SEM, EDX, and XPS analyses of the electrospun fibers. Nano- $\text{TiO}_2$ -doped xylan-g-PMMA electrospun nanofibers were also obtained, and their photocatalytic activity for MB degradation was measured.

## 2. Materials and Methods

### 2.1. Materials and Chemicals

Xylan used in this study was isolated from wheat straw by the alkaline peroxide method [32], which has a weight-average molecular weight of  $18,350 \text{ g mol}^{-1}$ . The isolated xylan was purified with 75% ethanol-water solution and then dried at  $60^\circ\text{C}$  for 24 h in a vacuum oven. N, N-Dimethylformamide (DMF) and MMA were purchased from J&K Scientific Co., Ltd. in Beijing, China and ammonium persulfate ( $(\text{NH}_4)_2\text{S}_2\text{O}_8$ ) and sodium sulfite ( $\text{Na}_2\text{SO}_3$ ) were purchased from Tianjin Hongyan Chemical Reagent Factory in China.  $\text{TiO}_2$  nanoparticles of 30 nm were supplied by ST-NANO SCIENCE & TECHNOLOGY Co., Ltd., Shanghai, China. All chemical reagents were of analytical grade.

### 2.2. Synthesis of Xylan-g-PMMA

The xylan-g-PMMA were synthesized from xylan and MMA by using ammonium persulfate ( $(\text{NH}_4)_2\text{S}_2\text{O}_8$ ) and sodium sulfite ( $\text{Na}_2\text{SO}_3$ ) as a catalytic system. Xylan (2000 mg) was first dissolved in deionized water (40 mL) at room temperature, and subsequently, DMF (40 mL) was added. Then, the mixture was placed in a rotary evaporator to remove the deionized water at  $50^\circ\text{C}$ . After adding lithium chloride (400 mg), it was stirred to acquire a homogeneous solution. For the synthesis of xylan-g-PMMA, the xylan solution was kept in a  $50^\circ\text{C}$  water bath, in which  $(\text{NH}_4)_2\text{S}_2\text{O}_8$  (50 mg) and  $\text{Na}_2\text{SO}_3$  (50 mg) were added, stirring for 5 min. MMA was added to the mixture at different AXU/MMA molar ratios of 1:2, 1:4, 1:6, and 0:10 and stirred for 6 h at  $50^\circ\text{C}$ . At the end of the reaction, the mixture was poured slowly into excess ethanol and filtered. This was followed by drying the product in vacuo for 12 h to obtain a solid.

### 2.3. Viscosity Measurement and Structural Characterizations

Xylan-g-PMMA (500 mg) was mixed with different ratios of xylan: MMA was dissolved in a mixture of DMF (5 mL) and chloroform (1 mL) at room temperature, respectively. Shear viscosity ( $\eta$ ) values for the xylan-g-PMMA solutions were obtained from an NDJ-79A rotational viscometer (Changji Geological Instrument Co., Ltd., Shanghai, China) at room temperature.

FT-IR spectra of the xylan and xylan-g-PMMA were recorded by a Nicolet 510 spectrophotometer (Thermo Scientific, Waltham, MA, USA) in the  $4000\text{--}400 \text{ cm}^{-1}$  region.  $^1\text{H}$ ,  $^{13}\text{C}$  heteronuclear single-quantum coherence (HSQC) NMR spectra were recorded by a Bruker AVANCE spectrophotometer (400 MHz), and 50 mg of dried xylan-g-PMMA with AXU/MMA at a molar ratio of 1:4 was dissolved in 0.5 mL of dimethyl sulfoxide- $d_6$  ( $\text{DMSO-}d_6$ ) at  $40^\circ\text{C}$  and recorded at room temperature. All chemical shifts were relative to

the resonance of tetramethylsilane (TMS,  $\delta = 0$ ). Electrospun fibers' images were obtained by using a VEGA 3 LMH SEM microscope (TESCAN, Brno, Czech Republic) at 10 kV after being transferred to an SEM stud and coated with gold.

#### 2.4. Electrospinning

Electrospun fibers were fabricated by a 500 mg xylan-g-PMMA solution using an SS-2534H electrospinning device (Ucalery, Co., Ltd., Beijing, China) at 15 kV under room temperature and 20% humidity. Various xylan-g-PMMA solutions were placed in a 5 mL syringe with a metal needle (0.81 mm  $\times$  0.51 mm), respectively. Electrospun fibers were collected on aluminum foil.

#### 2.5. The Preparation of Electrospun Xylan-g-PMMA/TiO<sub>2</sub> Fibers

TiO<sub>2</sub> nanoparticles were added to the solutions of xylan-g-PMMA with different mass ratios of 0%, 10%, and 30%. To reduce the loss of TiO<sub>2</sub> loaded on the electrospun fibers in the further application, triethoxyvinylsilane was added into the spun liquid in the mass ratio of 62%, to TiO<sub>2</sub>. The well-dispersed mixtures were electrospun at the optimal condition for 30 min according to Section 2.4. The electrospun fibers were obtained on aluminum foil and characterized by the VEGA 3 LMH SEM microscope and INCA X-ACT energy dispersive spectroscopy (Oxford, UK).

#### 2.6. Photocatalytic Degradation Property of Electrospun Xylan-g-PMMA/TiO<sub>2</sub> Fibers

MB aqueous solutions of 0.1, 0.2, 0.3, 0.4, and 0.5 mg/L were prepared, and their absorbance values were measured by an ultraviolet spectrophotometer (752B, Tianjin Precise Instrument Co., Ltd., Tianjin, China) at 665 nm. The standard curve was obtained by linear-fitting the values,  $A = 0.094c + 0.0402$ , and the linear correlation coefficient was 0.99759.

Then, 20 mg/L of MB aqueous solution was used for photocatalytic degradation. The electrospun xylan-g-PMMA/TiO<sub>2</sub> fibers collected on aluminum foil were cut into the mats of 6  $\times$  2.5 cm<sup>2</sup>, then put into 30 mL of MB aqueous solution under the irradiation of 125 W ultraviolet light (365–400 nm; Ausbond, China) with a distance of 5 cm between the light and the surface of the solutions. The absorbance values of the MB aqueous solutions were detected at 665 nm every 30 min by using the ultraviolet spectrophotometer. The MB photocatalytic degradation rate (DR) was calculated by the equation of  $DR = (c_0 - c)/c_0$ , where  $c_0$  stands for the initial concentration of the MB aqueous solution.

### 3. Results

#### 3.1. FT-IR Analysis

Due to the vibration or rotation of different functional groups and chemical bonds, they absorb infrared light at different wavelengths. Accordingly, FT-IR can be used to determine which functional groups or chemical bonds are present or changed in a sample, and for qualitative, quantitative, and reaction process studies of substances [78,79]. To further understand the chemical bond and group changes of xylan and xylan-G-PMMA, the samples were analyzed by FT-IR. The FT-IR spectra of xylan and xylan-g-PMMA (the AXU/MMA molar ratio is 1:4) are shown in Figure 1. The infrared spectrum of xylan polymer displays a broad absorption band at 3419 cm<sup>-1</sup> that is attributed to OH stretching associated with polar groups linking through intra- and inter-molecular hydrogen bonding [80]. The absorptions around 2921 and 1428 cm<sup>-1</sup> correspond to C-H stretching and bending vibration of CH<sub>2</sub> in the molecule. The absorption at 1637 cm<sup>-1</sup> owes to the absorbed water in the sample. The absorption at 1117 cm<sup>-1</sup> arises from the stretching vibration of C-C in the xylan polymer, and the absorption at 1041 cm<sup>-1</sup> results from the bending vibration of C-OH [81]. These main characteristic absorptions were also observed in the infrared spectrum of the xylan-g-PMMA. Particularly, the absorption peak at 1729 cm<sup>-1</sup> was typically observed in the xylan-g-PMMA spectrum, which is associated with C=O

stretching of the methoxycarbonyl group [82,83]. All these results indicated the successful graft copolymerization of xylan and MMA.

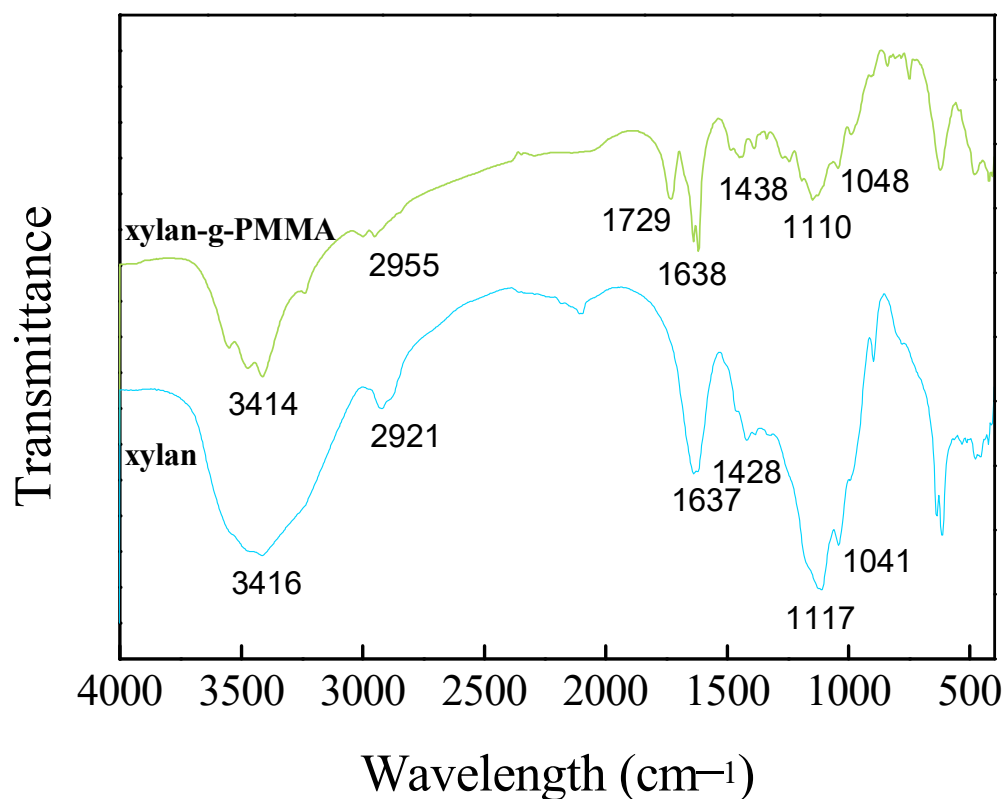


**Figure 1.** FT-IR spectra of xylan and xylan-g-PMMA.

### 3.2. NMR Analysis

Figure 2 presents the  $^1\text{H}$ - $^{13}\text{C}$  HSQC NMR spectrum of the xylan-g-PMMA (the AXU/MMA molar ratio is 1:4), and the vertical axis (f1) denotes  $^{13}\text{C}$  NMR chemical shifts ( $\delta_{\text{C}}$ ) while the horizontal axis (f2) denotes  $^1\text{H}$  NMR chemical shifts ( $\delta_{\text{H}}$ ). As marked in Figure 2, the attributions of those signals were: ( $\delta_{\text{C}}, \delta_{\text{H}}$ ) (100.94, 4.20): (C1, H); (74.91, 3.44): (C2, H); (73.40, 3.19): (C3, H); (71.87, 2.97): (C4, H); (62.58, 3.84/3.19): (C5, H<sub>a</sub>/H<sub>b</sub>); (45.59, 2.50): (C6, H<sub>2</sub>); (15.34, 0.68): (C8, H<sub>3</sub>); (61.07, 3.41): (C10, H<sub>3</sub>) [33,84,85]. The strong signals at (39.52, 2.56) ppm and (51.00, 3.53) ppm were derived from the solvent DMSO and the absorbed water in the sample, respectively. No protons connected with C7 and C9 resulted in no signals shown in the 2D spectrum in Figure 2. The chemical shifts were recorded at 44.32 and 177.70 ppm in the  $^{13}\text{C}$  NMR spectrum, corresponding to C6 and C9, respectively. These typical signals detected in the HSQC NMR spectrum demonstrated the targeted synthesis of xylan-g-PMMA.

### 3.3. Polymer Solution Viscosity

Various xylan-g-PMMA solutions with AXU/MMA molar ratios of 1:2, 1:4, 1:6, and 0:10 were prepared in the mixed solvent of DMF and chloroform, with the weight concentration of 7.42%. The viscosity data of the solutions at room temperature are shown in Figure 3. It illustrates that, when increasing MMA is added to the polymerization reaction, the solutions would become stickier. As the viscosity of a polymer (solution) has a strong positive correlation with its molecular weight, it can be concluded that the increase of added MMA content in the reaction contributed to the increase of the molecular weight of the products.

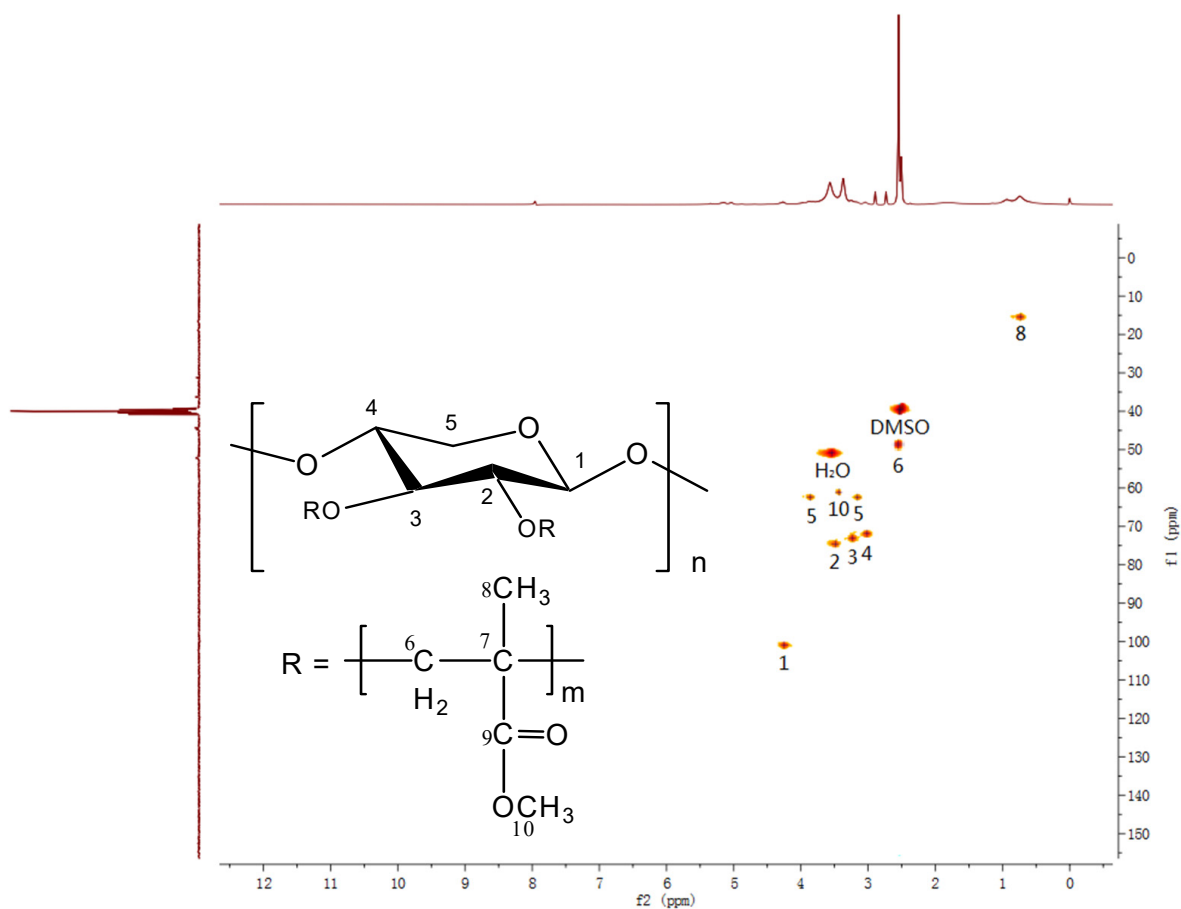


Figure 2.  $^1\text{H}$ - $^{13}\text{C}$  HSQC NMR spectrum of xylan-g-PMMA.

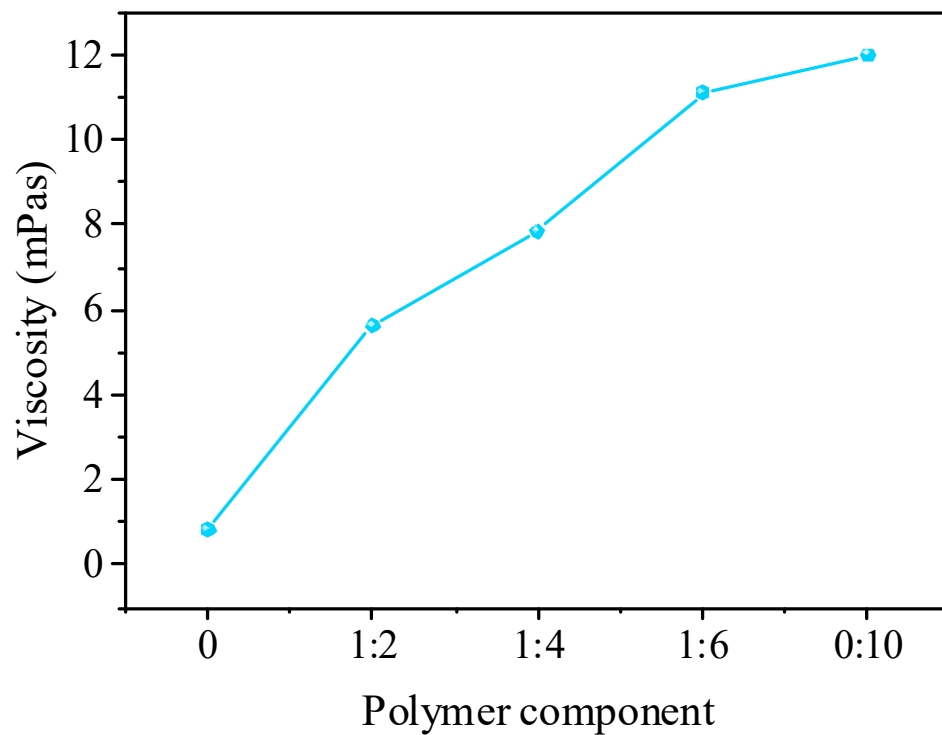
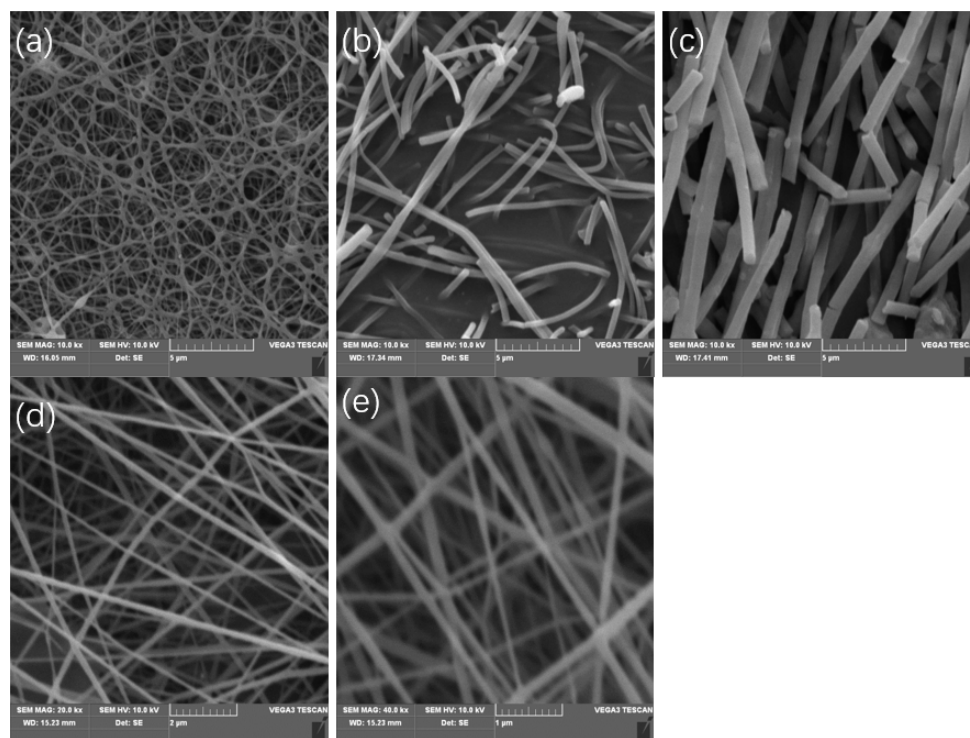


Figure 3. The viscosity of xylan-g-PMMA solutions with different AXU/MMA molar ratios.

### 3.4. Effect of Solvents on Electrospinning

The solvent is essential to solution electrospinning. As stated in the Introduction Section, the solvent should be equipped with appropriate volatility, with the boiling point in the range of 70 to 150 °C, in a normal experimental situation without any other remedies. Acetone had been tried in this study, which led to the interruption of the process since the needle of the syringe was jammed by the solidified copolymer. As a result of its good volatility, acetone in the flow evaporated too fast to keep enough fluidity in the flow before it was sprayed. DMF had been attempted as well because the xylan-g-PMMA could dissolve in it well. Instead of individual fibers, there were only some copolymer nets obtained, as shown in Figure 4a. This may be due to two reasons: the DMF solvent evaporated too slow to obtain the fibers with enough solidity and they became aggregated, and the large surface area of the fiber mats resulted in the excellent adsorption capacity of the solvent vaporized around the surface of the fiber mats, which made it possible for the redissolution of the fibers before the solvent was exhausted from the relatively isolated experimental equipment.



**Figure 4.** The SEM images of the fibers produced with the solvent of (a) pure DMF, (b) 5 mL of DMF + 2 mL of acetone, (c) 5 mL of DMF + 1 mL of acetone, (d) 5 mL of DMF + 1 mL of chloroform + 1 mL of acetone, and (e) 5 mL of DMF + 1 mL of chloroform. (a–c) 10 kx, (d,e) 20 kx.

To improve the volatility of DMF and prepare individual fibers, the mixed solvents were obtained by adding acetone to DMF in the volume ratio of 2:5, and the SEM image of the electrospun fibers is shown in Figure 4b. As can be seen, the fibers were broken into pieces. This may be the consequence of too much acetone added, as the fibers were solidified so much that they were easily broken. When decreasing the acetone added in DMF to a volume ratio of 1:5, the surface of the fibers became worse, being fragile and uneven, as shown in Figure 4c. This suggests that acetone may contribute to the dissolution of the product in the mixed solvent. Another solvent with a low boiling point, though higher than acetone, chloroform, was also attempted. When chloroform was added into the DMF in the volume ratio of 1:5, those problems were eliminated, as shown in Figure 4d,e.

In the comparison of the diameters of the electrospun fibers in Table 1, it is found that the diameters decreased with increasing the added solvent ratio with a low boiling

point: acetone or chloroform. This can be explained because adding more solvents into the solution reduced the concentration of the copolymer in solvents, which contributed to the decrease of the surface tension of the solutions. The less surface tension affecting the flow, the more intensively the fibers would be stretched. As an additive for DMF solution electrospinning, chloroform is more efficient than acetone to obtain fibers with enough tenacity and small diameters.

**Table 1.** The effect of solvents on the diameters of the electrospun fibers.

Molar Ratio of Xylan/MMA	Flow Speed/(mL/min)	Receiving Distance/cm	Solvents	Diameters of the Fibers/nm		
				Max.	Min.	Mean
1:4	0.05650	15	5 mL DMF + 1 mL acetone (c)	1184.83	596.61	744.52
			5 mL DMF + 2 mL acetone (b)	435.57	150.35	297.82
1:4	0.01130	10	5 mL DMF + 1 mL chloroform(e)	160.83	66.28	140.37
			5 mL DMF + 1 mL chloroform + 1 acetone (d)	130.82	63.05	99.41
1:6	0.00565	15	5 mL DMF + 1 mL chloroform	253.35	88.88	164.2
			5 mL DMF + 1 mL chloroform + 1 mL acetone	209.27	88.92	137.41

### 3.5. Effect of AXU/MMA Molar Ratio on Electrospinning

The molar ratio of AXU/MMA primarily has an impact on the molecular weight of the xylan-g-PMMA, which would remarkably affect the electrospinning process. The electrospinning process could not be conducted using the pure xylan or the xylan-g-PMMA with the minimal AXU/MMA molar ratio (1:2), and there were no fibers besides spray-deposited on the aluminum foil. When increasing the MMA ratio added in the polymerization reaction to the molar ratios of 1:4 and 1:6, plentiful fibers were collected on the foil, and the diameters of the fibers increased as well (Table 2 and Figure 5). In an extreme situation with a molar ratio of 0:10, the diameter of the fibers became the largest. These results correspond to the viscosity data of the polymers in Section 3.3. The more MMA added to the reaction, the larger the molecular weight of the products, and the internal resistance of the polymer solutions would become stronger against the electric field force, thus leading to the increase of the diameters of the fibers.

**Table 2.** The effect of AXU/MMA molar ratios on the diameters of the electrospun fibers.

Molar Ratio of Xylan/MMA	Solvent	Receiving Distance/cm	Flow Speed/(mL/min)	Diameters of the Fibers/nm		
				Max.	Min.	Mean
1:4	5 mL DMF + 1 mL chloroform	15	0.00565	179.79	70.72	125.25
1:6				253.35	88.88	164.2
0:10				362.25	162.3	227.95

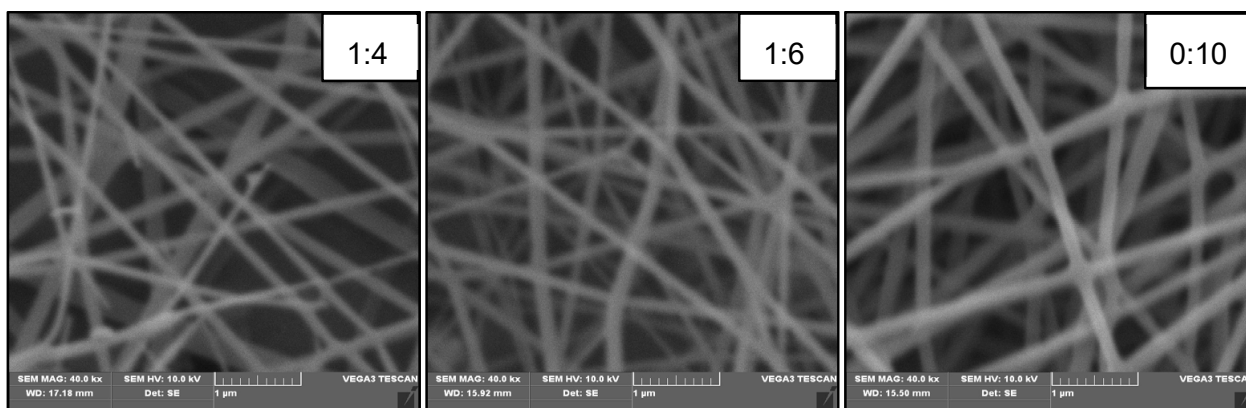


**Figure 5.** The SEM images (40 kx) of the electrospun fibers were produced with AXU/MMA molar ratios of 1:4, 1:6, and 0:10.

### 3.6. Effect of Flow Speed on Electrospinning

In the continuous electrospinning process, flow speed is an important operating parameter, which should be matched with the flow spraying speed in the high-voltage field, and the latter is correlated to the electrospinning voltage. In this study, the flow speed was set at different values, while the applied voltage was 15 kV. When the speed was lower than 0.00565 mL/min, the electrospinning spray became unstable as no sufficient flow was provided. When the speed was higher than 0.02260 mL/min, there were some fibers dropped from the needle of the syringe as there were too many liquids spraying to the receiver. However, in the tolerable range, no remarkable variations were observed on the fibers as the speed accelerated (Table 3).

**Table 3.** The effect of flow speed on diameters of the fibers.

Molar Ratio of Xylan/MMA	Solvent	Receiving Distance/cm	Flow Speed/(mL/min)	Diameters of the Fibers/nm		
				Max.	Min.	Mean
1:4	5 mL DMF + 1 mL chloroform	10	0.00565	162.79	58.90	111.90
			0.01130	140.85	68.28	108.22
			0.02260	160.83	66.28	109.36
1:6	5 mL DMF + 1 mL chloroform	15	0.00565	267.74	137.4	177.99
			0.01130	320.59	100.0	177.84
			0.02260	291.25	106.9	172.07

### 3.7. Effect of Receiving Distance on Electrospinning

The receiving distance could influence the electrostatic attraction of the flow, which would negatively affect the diameters of the fibers. It was found that when the receiving distance was less than 10 cm, the flow sprayed to the foil directly and no fibers were obtained as the electrostatic attraction was too strong. When the distance was beyond 15 cm, the weak attraction made it possible for the fibers to move with the flow of the air, and the fibers deposited unevenly on the receiving foil on a large scale, which was harmful to the collection of the fibers. After the comparison of the three different conditions (in Table 4), it could be concluded that the diameters of the fibers increased slightly with the increase of the acceptable receiving distance, which is consistent with the former study [86].

**Table 4.** The effect of receiving distance on diameters of the electrospun fibers.

Molar Ratio of Xylan/MMA	Solvent	Flow Speed/(mL/min)	Receiving Distance/cm	Diameters of the Fibers/nm		
				Max.	Min.	Mean
1:4	5 mL DMF + 1 mL chloroform	0.01130	10	160.83	66.28	109.36
			15	211.07	100.11	144.90
1:6	5 mL DMF + 1 mL chloroform	0.01130	10	194.77	84.36	122.72
			15	289.62	91.03	143.16
0:10	5 mL DMF + 1 mL chloroform	0.00565	10	391.64	138.68	251.02
			15	451.96	144.81	296.17

### 3.8. Photocatalytic Degradation of MB by Electrospun Xylan-g-PMMA/TiO<sub>2</sub> Fibers

According to the above discussions, electrospun xylan-g-PMMA/TiO<sub>2</sub> fibers were prepared at the following electrospinning parameters: the DMF and chloroform mixed solvent in a volume ratio of 5:1, receiving distance of 10 cm, and flow speed of 0.00565 mL/min. Figure 6a presents the SEM image of the electrospun xylan-g-PMMA/TiO<sub>2</sub> fibers, and it shows that the electrospun xylan-g-PMMA/TiO<sub>2</sub> nanofibers were well-prepared, and the presence of some nodes could be considered to be the aggregated TiO<sub>2</sub> linked with triethoxyvinylsilane, which was proven by the X-ray EDS spectrum (Figure 6b). There is the presence of a Si signal in the EDS spectrum, which was due to triethoxyvinylsilane. To reduce the loss of TiO<sub>2</sub> loaded on the electrospun fibers, triethoxyvinylsilane was added into the spun liquid.

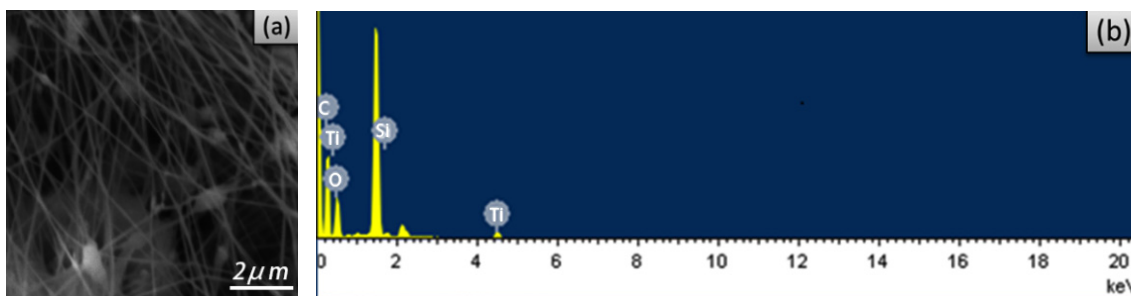


Figure 6. SEM image (a) and EDX spectrum (b) of electrospun xylan-g-PMMA/TiO<sub>2</sub> fibers.

XPS analysis of electrospun xylan-g-PMMA/TiO<sub>2</sub> fibers was also performed (Figure 7), and it identified the peaks of Ti, Si, O, and C. The XPS spectrum of Si2p of electrospun xylan-g-PMMA/TiO<sub>2</sub> fibers showed that Si mainly existed in two forms (Figure 8). The two peaks of binding energy, EB, at 102.58 and 100.88 eV corresponded to Si-O and Si-C peaks [87,88], respectively, indicating that triethoxyvinylsilane reacted with O atoms on the surface of TiO<sub>2</sub> (Figure 9). This is because the surface of nano-TiO<sub>2</sub> contains a large number of hydroxyl groups, and the -Si(OH)<sub>3</sub> generated by the hydrolysis of -Si(OC<sub>2</sub>H<sub>5</sub>)<sub>3</sub> in triethoxyvinylsilane can react with hydroxyl groups, making triethoxyvinylsilane chemically bonded to the surface of nano-TiO<sub>2</sub> to form Ti-O-Si bonds.

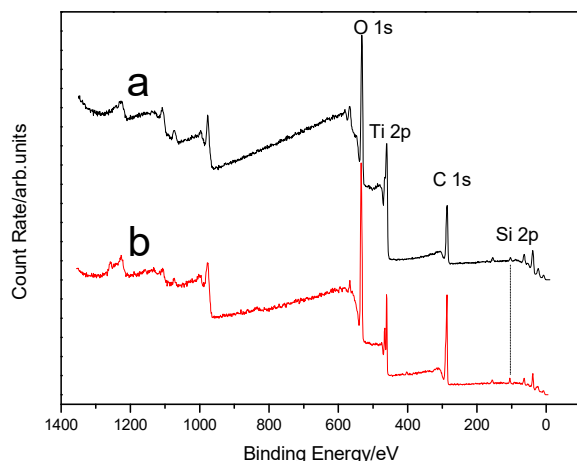


Figure 7. XPS spectra of electrospun xylan/TiO<sub>2</sub> fibers (a, 10%; b, 30%).

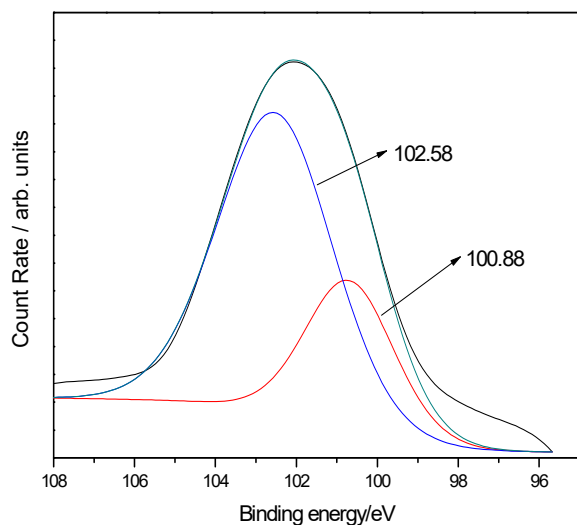


Figure 8. XPS spectrum of Si2p.



#### 4. Conclusions

Xylan is an important bioactive polysaccharide in nature, but the fabrication of electrospun xylan fibers is very difficult because of its low molecular weight and solubility. To prepare electrospun xylan fibers, xylan-g-PMMA were synthesized by copolymerization of MMA and xylan with a catalytic system of  $(\text{NH}_4)_2\text{S}_2\text{O}_8$  and  $\text{Na}_2\text{SO}_3$ , and electrospun fibers were prepared by solution electrospinning of xylan-g-PMMA. The mixture of DMF and chloroform in the volume ratio of 5:1, the AXU/MMA molar ratio lower than 1:2, the flow speed of 0.00565–0.02260 mL/min, and the receiving distance of 10–15 cm were found as the optimum operating parameters for electrospinning at the voltage of 15 kV by assessing the electrospinning process and the morphology of the fibers, and the diameters of the fibers increased with increasing the MMA content added in the copolymerization, the DMF content in the solvent, and the receiving distance.

$\text{TiO}_2$  nanoparticles were loaded in the electrospun xylan-g-PMMA nanofibers at the electrospinning parameters: DMF and chloroform mixed solvent in the volume ratio of 5:1, receiving distance of 10 cm, and flow speed of 0.00565 mL/min. The SEM image and X-ray EDS spectrum proved the successful loading of  $\text{TiO}_2$  on the fibers. The xylan-g-PMMA/ $\text{TiO}_2$  fibers showed good potential in photocatalytic degradation of MB dye. Additionally, this work demonstrates the first use of xylan to fabricate the nanofibers by electrospinning, which will provide a new direction to prepare nanomaterials with xylan. Furthermore, it may offer a novel strategy for the utilization of natural polymers to synthesize high efficiency, environmental, and economic photocatalysis for water treatment.

**Author Contributions:** Conceptualization, Y.X. and X.-F.S.; methodology, X.-F.S.; software, Y.X., W.L. and J.H.; validation, R.S.; formal analysis, S.H. and Y.W.; investigation, Y.X., W.L. and J.H.; resources, X.-F.S., R.S., S.H. and Y.W.; data curation, Y.X.; writing—original draft preparation, Y.X. and X.-F.S.; writing review and editing, Y.X. and X.-F.S.; visualization, W.L. and J.H.; supervision, X.-F.S.; project administration, X.-F.S.; funding acquisition, R.S. and W.L. All authors have read and agreed to the published version of the manuscript.

**Funding:** This research was funded by the Shenzhen Science and Technology Project for Sustainable Development (No. KCXFZ20201221173004012) and the National College Students Innovation and Entrepreneurship Training Program (202110699137).

**Institutional Review Board Statement:** Not applicable.

**Informed Consent Statement:** Not applicable.

**Data Availability Statement:** The data presented in this study are available upon request from the corresponding author.

**Conflicts of Interest:** The authors declare no conflict of interest.

#### References

1. Bhardwaj, N.; Kundu, S.C. Electrospinning: A fascinating fiber fabrication technique. *Biotechnol. Adv.* **2010**, *28*, 325–347. [[CrossRef](#)] [[PubMed](#)]
2. Rahmati, M.; Mills, D.K.; Urbanska, A.M.; Saeb, M.R.; Venugopal, J.R.; Ramakrishna, S.; Mozafari, M. Electrospinning for tissue engineering applications. *Prog. Mater. Sci.* **2021**, *117*, 100721. [[CrossRef](#)]
3. Zeleny, J. The electrical discharge from liquid points, and a hydrostatic method of measuring the electric intensity at their surfaces. *Phys. Rev.* **1914**, *3*, 69–91. [[CrossRef](#)]
4. Formahls, A. Process and Apparatus for Preparing Artificial Threads. U.S. Patent 1975504, 10 February 1934.
5. Taylor, G. Electrically Driven Jets. *Proc. R. Soc. Lon. Ser.-A* **1969**, *313*, 453–475.
6. Xue, J.; Wu, T.; Dai, Y.; Xia, Y. Electrospinning and electrospun nanofibers: Methods, materials, and applications. *Chem. Rev.* **2019**, *119*, 5298–5415. [[CrossRef](#)]
7. Ognibene, G.; Gangemi, C.M.A.; Spitaleri, L.; Gulino, A.; Purrello, R.; Cicala, G.; Fragala, M.E. Role of the surface composition of the polyethersulfone-TiIP- $\text{H}_2\text{T}_4$  fibers on lead removal: From electrostatic to coordinative binding. *J. Mater. Sci.* **2019**, *54*, 8023–8033. [[CrossRef](#)]
8. Yoon, J.; Yang, H.S.; Lee, B.S.; Yu, W.R. Recent progress in coaxial electrospinning: New parameters, various structures, and wide applications. *Adv. Mater.* **2018**, *30*, 1704765. [[CrossRef](#)]

9. Avossa, J.; Herwig, G.; Toncelli, C.; Itef, F.; Rossi, R.M. Electrospinning based on benign solvents: Current definitions, implications and strategies. *Green Chem.* **2022**, *24*, 2347–2375. [[CrossRef](#)]
10. Bombin, A.D.J.; Dunne, N.J.; McCarthy, H.O. Electrospinning of natural polymers for the production of nanofibres for wound healing applications. *Mater. Sci. Eng. C* **2020**, *114*, 110994. [[CrossRef](#)]
11. Pakravan, M.; Heuzey, M.C.; Aji, A. Core-shell structured PEO-chitosan nanofibers by coaxial electrospinning. *Biomacromolecules* **2012**, *13*, 412–421. [[CrossRef](#)]
12. Jing, Z.; Xu, X.Y.; Chen, X.S.; Liang, Q.Z.; Bian, X.C.; Yang, L.X.; Jing, X.B. Biodegradable electrospun fibers for drug delivery. *J. Control. Release* **2003**, *92*, 227–231.
13. Zhou, H.J.; Green, T.B.; Joo, Y.L. The thermal effects on electrospinning of polylactic acid melts. *Polymer* **2006**, *47*, 7497–7505. [[CrossRef](#)]
14. Kim, C.; Park, S.H.; Cho, J.K.; Lee, D.Y.; Park, T.J.; Lee, W.J.; Yang, K.S. Raman spectroscopic evaluation of polyacrylonitrile-based carbon nanofibers prepared by electrospinning. *J. Raman Spectrosc.* **2004**, *35*, 928–933. [[CrossRef](#)]
15. Nirmala, R.; Navamathavan, R.; Park, S.J.; Kim, H.Y. Recent Progress on the Fabrication of Ultrafine Polyamide-6 Based Nanofibers Via Electro-spinning: A Topical Review. *Nano-Micro Lett.* **2014**, *6*, 19. [[CrossRef](#)]
16. Reneker, D.H.; Kataphinan, W.; Theron, A.; Zussman, E.; Yarin, A.L. Nanofiber garlands of polycaprolactone by electrospinning. *Polymer* **2002**, *43*, 6785–6794. [[CrossRef](#)]
17. Acarer, S.; Pir, I.; Tufekci, M.; Turkoglu Demirkol, G.; Tufekci, N. Manufacturing and characterisation of polymeric membranes for water treatment and numerical investigation of mechanics of nanocomposite membranes. *Polymers* **2021**, *13*, 1661. [[CrossRef](#)]
18. Zheng, J.F.; He, A.H.; Li, J.X.; Han, C.C. Polymorphism control of poly(vinylidene fluoride) through electrospinning. *Macromol. Rapid Commun.* **2007**, *28*, 2159–2162. [[CrossRef](#)]
19. Gangemi, C.M.A.; Iudici, M.; Spitaleri, L.; Randazzo, R.; Gaeta, M.; D’Urso, A.; Gulino, A.; Purrello, R.; Fragala, M.E. Polyether-sulfone mats functionalized with porphyrin for removal of para-nitroaniline from aqueous solution. *Molecules* **2019**, *24*, 3344. [[CrossRef](#)]
20. Boland, E.D.; Matthews, J.A.; Pawlowski, K.J.; Simpson, D.G.; Wnek, G.E.; Bowlin, G.L. Electrospinning collagen and elastin: Preliminary vascular tissue engineering. *Front. Biosci.* **2004**, *9*, 1422–1432. [[CrossRef](#)]
21. Geng, X.Y.; Kwon, O.H.; Jang, J.H. Electrospinning of chitosan dissolved in concentrated acetic acid solution. *Biomaterials* **2005**, *26*, 5427–5432. [[CrossRef](#)]
22. Xu, S.S.; Zhang, J.; He, A.H.; Li, J.X.; Zhang, H.; Han, C.C. Electrospinning of native cellulose from nonvolatile solvent system. *Polymer* **2008**, *49*, 2911–2917. [[CrossRef](#)]
23. Pascu, E.I.; Stokes, J.; McGuinness, G.B. Electrospun composites of PHBV, silk fibroin and nano-hydroxyapatite for bone tissue engineering. *Mat. Sci. Eng. C-Mater.* **2013**, *33*, 4905–4916. [[CrossRef](#)] [[PubMed](#)]
24. Devadas, S.; Al-Ajrash, S.M.N.; Klosterman, D.A.; Crosson, K.M.; Crosson, G.S.; Vasquez, E.S. Fabrication and characterization of electrospun poly(acrylonitrile-co-methyl acrylate)/lignin nanofibers: Effects of lignin type and total polymer concentration. *Polymers* **2021**, *13*, 992. [[CrossRef](#)] [[PubMed](#)]
25. Shi, S.; Si, Y.; Han, Y.; Wu, T.; Iqbal, M.I.; Fei, B.; Li, R.K.; Hu, J.; Qu, J. Recent progress in protective membranes fabricated via electrospinning: Advanced materials, biomimetic structures, and functional applications. *Adv. Mater.* **2021**, *34*, 2107938. [[CrossRef](#)] [[PubMed](#)]
26. Soares, R.M.D.; Siqueira, N.M.; Prabhakaram, M.P.; Ramakrishna, S. Electrospinning and electrospay of bio-based and natural polymers for biomaterials development. *Mater. Sci. Eng. C Mater. Biol. Appl.* **2018**, *92*, 969–982. [[CrossRef](#)]
27. Wang, F.D.; Hu, S.; Jia, Q.X.; Zhang, L.Q. Advances in electrospinning of natural biomaterials for wound dressing. *J. Nanomater.* **2020**, *2020*, 8719859. [[CrossRef](#)]
28. Rostamabadi, H.; Assadpour, E.; Tabarestani, H.S.; Falsafi, S.R.; Jafari, S.M. Electrospinning approach for nanoencapsulation of bioactive compounds; recent advances and innovations. *Trends Food Sci. Technol.* **2020**, *100*, 190–209. [[CrossRef](#)]
29. Cunha, A.G.; Gandini, A. Turning polysaccharides into hydrophobic materials: A critical review. Part 1. Cellulose. *Cellulose* **2010**, *17*, 875–889. [[CrossRef](#)]
30. Sun, X.F.; Zhang, T.; Wang, H.H. Hemicelluloses-based hydrogels. In *Plant and Algal Hydrogels for Drug Delivery and Regenerative Medicine*; Giri, T.K., Ghosh, B., Eds.; Woodhead Publishing: Sawston, UK, 2021; pp. 181–216.
31. Luo, Y.P.; Li, Z.; Li, X.L.; Liu, X.F.; Fan, J.J.; Clark, J.H.; Hu, C.W. The production of furfural directly from hemicellulose in lignocellulosic biomass: A review. *Catal. Today* **2019**, *319*, 14–24. [[CrossRef](#)]
32. Berglund, J.; Mikkelsen, D.; Flanagan, B.M.; Dhital, S.; Gaunitz, S.; Henriksson, G.; Lindstrom, M.E.; Yakubov, G.E.; Gidley, M.J.; Vilaplana, F. Wood hemicelluloses exert distinct biomechanical contributions to cellulose fibrillar networks. *Nat. Commun.* **2020**, *11*, 4692. [[CrossRef](#)]
33. Sun, X.F.; Sun, R.C.; Fowler, P.; Baird, M.S. Extraction and characterization of original lignin and hemicelluloses from wheat straw. *J. Agric. Food Chem.* **2005**, *53*, 860–870. [[CrossRef](#)] [[PubMed](#)]
34. da Silva, A.E.; Marcelino, H.R.; Gomes, M.C.S.; Oliveira, E.E.; Nagashima, T., Jr.; Egito, E.S.T. Xylan, a promising hemicellulose for pharmaceutical use. In *Products and Applications of Biopolymers*; Verbeek, C.J.R., Ed.; InTechOpen: London, UK, 2012; pp. 61–84. ISBN 978-953-51-0226-7.
35. Naidu, D.S.; Hlangothi, S.P.; John, M.J. Bio-based products from xylan: A review. *Carbohydr. Polym.* **2018**, *179*, 28–41. [[CrossRef](#)] [[PubMed](#)]

36. Petzold-Welcke, K.; Schwikal, K.; Daus, S.; Heinze, T. Xylan derivatives and their application potential—Mini-review of own results. *Carbohydr. Polym.* **2014**, *100*, 80–88. [[CrossRef](#)] [[PubMed](#)]
37. Grondahl, M.; Eriksson, L.; Gatenholm, P. Material properties of plasticized hardwood xylans for potential application as oxygen barrier films. *Biomacromolecules* **2004**, *5*, 1528–1535. [[CrossRef](#)]
38. Moure, A.; Gullon, P.; Dominguez, H.; Parajo, J.C. Advances in the manufacture, purification and applications of xylo-oligosaccharides as food additives and nutraceuticals. *Process Biochem.* **2006**, *41*, 1913–1923. [[CrossRef](#)]
39. Fu, C.L.; Dong, X.B.; Wang, S.J.; Kong, F.G. Synthesis of nanocomposites using xylan and graphite oxide for remediation of cationic dyes in aqueous solutions. *Int. J. Biol. Macromol.* **2019**, *137*, 886–894. [[CrossRef](#)]
40. Kamdem, D.P.; Shen, Z.; Nabinejad, O.; Shu, Z.J. Development of biodegradable composite chitosan-based films incorporated with xylan and carvacrol for food packaging application. *Food Packag. Shelf Life* **2019**, *21*, 100344. [[CrossRef](#)]
41. Rao, J.; Lv, Z.; Chen, G.; Hao, X.; Guan, Y.; Peng, F. Fabrication of flexible composite film based on xylan from pulping process for packaging application. *Int. J. Biol. Macromol.* **2021**, *173*, 285–292. [[CrossRef](#)]
42. Sauraj; Kumar, S.U.; Kumar, V.; Priyadarshi, R.; Gopinath, P.; Negi, Y.S. pH-responsive prodrug nanoparticles based on xylan-curcumin conjugate for the efficient delivery of curcumin in cancer therapy. *Carbohydr. Polym.* **2018**, *188*, 252–259. [[CrossRef](#)]
43. Ali, A.; Hasan, A.; Negi, Y.S. Effect of cellulose nanocrystals on xylan/chitosan/nano $\beta$ -TCP composite matrix for bone tissue engineering. *Cellulose* **2022**, *29*, 5689–5709. [[CrossRef](#)]
44. Wu, J.; Wang, N.; Zhao, Y.; Jiang, L. Electrospinning of multilevel structured functional micro-/nanofibers and their applications. *J. Mater. Chem. A* **2013**, *1*, 7290–7305. [[CrossRef](#)]
45. Baji, A.; Mai, Y.W.; Wong, S.C.; Abtahi, M.; Chen, P. Electrospinning of polymer nanofibers: Effects on oriented morphology, structures and tensile properties. *Compos. Sci. Technol.* **2010**, *70*, 703–718. [[CrossRef](#)]
46. Zhang, C.Q.; Lu, R.H.; Liu, C.; Yuan, L.; Wang, J.; Zhao, Y.; Yu, C.Z. High yield electrosynthesis of hydrogen peroxide from water using electrospun CaSnO<sub>3</sub>@carbon fiber membrane catalysts with abundant oxygen vacancy. *Adv. Funct. Mater.* **2021**, *31*, 2100099. [[CrossRef](#)]
47. Li, S.; Cui, Z.M.; Li, D.M.; Yue, G.C.; Liu, J.; Ding, H.G.; Gao, S.W.; Zhao, Y.C.; Wang, N.; Zhao, Y. Hierarchically structured electrospinning nanofibers for catalysis and energy storage. *Compos. Commun.* **2019**, *13*, 1–11. [[CrossRef](#)]
48. Lu, T.; Cui, J.; Qu, Q.; Wang, Y.; Zhang, J.; Xiong, R.; Ma, W.; Huang, C. Multistructured electrospun nanofibers for air filtration: A review. *ACS Appl. Mater. Interfaces* **2021**, *13*, 23293–23313. [[CrossRef](#)]
49. Deng, Y.K.; Lu, T.; Cui, J.X.; Samal, S.K.; Xiong, R.H.; Huang, C.B. Bio-based electrospun nanofiber as building blocks for a novel eco-friendly air filtration membrane: A review. *Sep. Purif. Technol.* **2021**, *277*, 119623. [[CrossRef](#)]
50. Khoshnevisan, K.; Maleki, H.; Samadian, H.; Shahsavari, S.; Sarrafzadeh, M.H.; Larijani, B.; Dorkoosh, F.A.; Haghpanah, V.; Khorramzadeh, M.R. Cellulose acetate electrospun nanofibers for drug delivery systems: Applications and recent advances. *Carbohydr. Polym.* **2018**, *198*, 131–141. [[CrossRef](#)]
51. Wu, J.; Zhang, Z.; Gu, J.; Zhou, W.; Liang, X.; Zhou, G.; Han, C.C.; Xu, S.; Liu, Y. Mechanism of a long-term controlled drug release system based on simple blended electrospun fibers. *J. Control. Release* **2020**, *320*, 337–346. [[CrossRef](#)]
52. Abutaleb, A. Catalytic and photocatalytic electrospun nanofibers for hydrogen generation from ammonia borane complex: A review. *Polymers* **2021**, *13*, 2290. [[CrossRef](#)]
53. Salmeri, M.; Ognibene, G.; Saitta, L.; Lombardo, C.; Genovese, C.; Barcellona, M.; D’Urso, A.; Spitaleri, L.; Blanco, I.; Cicala, G.; et al. Optimization of ZnO nanorods growth on polyethersulfone electrospun mats to promote antibacterial properties. *Molecules* **2020**, *25*, 1696. [[CrossRef](#)]
54. Xiao, B.Q.; Wang, W.; Zhang, X.; Long, G.B.; Fan, J.T.; Chen, H.X.; Deng, L. A novel fractal solution for permeability and Kozeny-Carman constant of fibrous porous media made up of solid particles and porous fibers. *Powder Technol.* **2019**, *349*, 92–98. [[CrossRef](#)]
55. Gunn, D.J. Transfer of heat or mass to particles in fixed and fluidized-beds. *Int. J. Heat Mass Transfer* **1978**, *21*, 467–476. [[CrossRef](#)]
56. Boudart, M. Catalysis by supported metals. *Adv. Catal.* **1969**, *20*, 153–166.
57. Navalón, S.; Herance, J.R.; Álvaro, M.; García, H. General aspects in the use of graphenes in catalysis. *Mater. Horiz.* **2018**, *5*, 363–378. [[CrossRef](#)]
58. Formo, E.; Lee, E.; Campbell, D.; Xia, Y. Functionalization of electrospun TiO<sub>2</sub> nanofibers with Pt nanoparticles and nanowires for catalytic applications. *Nano Lett.* **2008**, *8*, 668–672. [[CrossRef](#)] [[PubMed](#)]
59. Patel, A.C.; Li, S.X.; Wang, C.; Zhang, W.J.; Wei, Y. Electrospinning of porous silica nanofibers containing silver nanoparticles for catalytic applications. *Chem. Mater.* **2007**, *19*, 1231–1238. [[CrossRef](#)]
60. Guo, Q.; Zhou, C.; Ma, Z.; Yang, X. Fundamentals of TiO<sub>2</sub> photocatalysis: Concepts, mechanisms, and challenges. *Adv. Mater.* **2019**, *31*, e1901997. [[CrossRef](#)]
61. Meng, A.; Zhang, L.; Cheng, B.; Yu, J. Dual cocatalysts in TiO<sub>2</sub> photocatalysis. *Adv. Mater.* **2019**, *31*, e1807660. [[CrossRef](#)]
62. Ruan, X.; Cui, X.; Cui, Y.; Fan, X.; Li, Z.; Xie, T.; Ba, K.; Jia, G.; Zhang, H.; Zhang, L. Favorable energy band alignment of TiO<sub>2</sub> anatase/rutile heterophase homojunctions yields photocatalytic hydrogen evolution with quantum efficiency exceeding 45.6%. *Adv. Energy Mater.* **2022**, *12*, 2200298. [[CrossRef](#)]
63. Shayegan, Z.; Lee, C.S.; Haghghat, F. TiO<sub>2</sub> photocatalyst for removal of volatile organic compounds in gas phase—A review. *Chem. Eng. J.* **2018**, *334*, 2408–2439. [[CrossRef](#)]

64. Zimbone, M.; Cacciato, G.; Spitaleri, L.; Egdell, R.G.; Grimaldi, M.G.; Gulino, A. Sb-doped titanium oxide: A rationale for its photocatalytic activity for environmental remediation. *ACS Omega* **2018**, *3*, 11270–11277. [[CrossRef](#)] [[PubMed](#)]
65. Naldoni, A.; Altomare, M.; Zoppellaro, G.; Liu, N.; Kment, S.; Zboril, R.; Schmuki, P. Photocatalysis with reduced TiO<sub>2</sub>: From black TiO<sub>2</sub> to cocatalyst-free hydrogen production. *ACS Catal.* **2019**, *9*, 345–364. [[CrossRef](#)] [[PubMed](#)]
66. Kumaravel, V.; Mathew, S.; Bartlett, J.; Pillai, S.C. Photocatalytic hydrogen production using metal doped TiO<sub>2</sub>: A review of recent advances. *Appl. Catal. B* **2019**, *244*, 1021–1064. [[CrossRef](#)]
67. Fang, S.; Liu, Y.; Sun, Z.; Lang, J.; Bao, C.; Hu, Y.H. Photocatalytic hydrogen production over Rh-loaded TiO<sub>2</sub>: What is the origin of hydrogen and how to achieve hydrogen production from water? *Appl. Catal. B* **2020**, *278*, 119316. [[CrossRef](#)]
68. Kusiak-Nejman, E.; Morawski, A.W. TiO<sub>2</sub>/graphene-based nanocomposites for water treatment: A brief overview of charge carrier transfer, antimicrobial and photocatalytic performance. *Appl. Catal. B* **2019**, *253*, 179–186. [[CrossRef](#)]
69. Yang, X.J.; Sun, H.W.; Li, G.Y.; An, T.C.; Choi, W.Y. Fouling of TiO<sub>2</sub> induced by natural organic matters during photocatalytic water treatment: Mechanisms and regeneration strategy. *Appl. Catal. B* **2021**, *294*, 120252. [[CrossRef](#)]
70. Shehzad, N.; Tahir, M.; Johari, K.; Murugesan, T.; Hussain, M. A critical review on TiO<sub>2</sub> based photocatalytic CO<sub>2</sub> reduction system: Strategies to improve efficiency. *J. CO<sub>2</sub> Util.* **2018**, *26*, 98–122. [[CrossRef](#)]
71. Xiong, Z.; Lei, Z.; Li, Y.Z.; Dong, L.C.; Zhao, Y.C.; Zhang, J.Y. A review on modification of facet-engineered TiO<sub>2</sub> for photocatalytic CO<sub>2</sub> reduction. *J. Photochem. Photobiol. C* **2018**, *36*, 24–47. [[CrossRef](#)]
72. Wang, L.B.; Cheng, B.; Zhang, L.Y.; Yu, J.G. In situ irradiated XPS investigation on S-scheme TiO<sub>2</sub>@ZnIn<sub>2</sub>S<sub>4</sub> photocatalyst for efficient photocatalytic CO<sub>2</sub> reduction. *Small* **2021**, *17*, 2103447. [[CrossRef](#)]
73. Kaplan, R.; Erjavec, B.; Pintar, A. Enhanced photocatalytic activity of single-phase, nanocomposite and physically mixed TiO<sub>2</sub> polymorphs. *Appl. Catal. A-Gen.* **2015**, *489*, 51–60. [[CrossRef](#)]
74. Fiorenza, R.; Bellardita, M.; Balsamo, S.A.; Spitaleri, L.; Gulino, A.; Condorelli, M.; D'Urso, L.; Scirè, S.; Palmisano, L. A solar photothermocatalytic approach for the CO<sub>2</sub> conversion: Investigation of different synergisms on CoO-CuO/brookite TiO<sub>2</sub>-CeO<sub>2</sub> catalysts. *Chem. Eng. J.* **2022**, *428*, 131249. [[CrossRef](#)]
75. Diebold, U. The surface science of titanium dioxide. *Surf. Sci. Rep.* **2003**, *48*, 53–229. [[CrossRef](#)]
76. Linsebigler, A.L.; Lu, G.Q.; Yates, J.T. Photocatalysis on TiO<sub>2</sub> surfaces—principles, mechanisms, and selected results. *Chem. Rev.* **1995**, *95*, 735–758. [[CrossRef](#)]
77. Fujishima, A.; Vitae, T.N.R.; Tryk, D.A. Titanium dioxide photocatalysis. *J. Photochem. Photobiol. C Photochem. Rev.* **2000**, *1*, 21. [[CrossRef](#)]
78. Wright, S.L.; Kelly, F.J. Plastic and human health: A micro issue? *Environ. Sci. Technol.* **2017**, *51*, 6634–6647. [[CrossRef](#)] [[PubMed](#)]
79. Gulino, A.; Papanikolaou, G.; Lanzafame, P.; Aaliti, A.; Primerano, P.; Spitaleri, L.; Triolo, C.; Dahrouch, Z.; Khaskhoussi, A.; Lo Schiavo, S. Synthesis, characterization and photocatalytic behavior of SiO<sub>2</sub>@nitrided-TiO<sub>2</sub> nanocomposites obtained by a straightforward novel approach. *Chemistryopen* **2021**, *10*, 1033–1040. [[CrossRef](#)] [[PubMed](#)]
80. Sun, R.C.; Fang, J.M.; Goodwin, A.; Lawther, J.M.; Bolton, A.J. Fractionation and characterization of polysaccharides from abaca fibre. *Carbohydr. Polym.* **1998**, *37*, 351–359. [[CrossRef](#)]
81. Shan, S.; Sun, X.-F.; Xie, Y.; Li, W.; Ji, T. High-performance hydrogel adsorbent based on cellulose, hemicellulose, and lignin for copper(II) ion removal. *Polymers* **2021**, *13*, 3063. [[CrossRef](#)]
82. Delekar, S.D.; Dhodamani, A.G.; More, K.V.; Dongale, T.D.; Kamat, R.K.; Acquah, S.F.A.; Dalal, N.S.; Panda, D.K. Structural and optical properties of nanocrystalline TiO<sub>2</sub> with multiwalled carbon nanotubes and its photovoltaic studies using Ru(II) sensitizers. *ACS Omega* **2018**, *3*, 2743–2756. [[CrossRef](#)] [[PubMed](#)]
83. Fiorenza, R.; Di Mauro, A.; Cantarella, M.; Iaria, C.; Scalisi, E.M.; Brundo, M.V.; Gulino, A.; Spitaleri, L.; Nicotra, G.; Dattilo, S.; et al. Preferential removal of pesticides from water by molecular imprinting on TiO<sub>2</sub> photocatalysts. *Chem. Eng. J.* **2020**, *379*, 122309. [[CrossRef](#)]
84. Brar, A.S.; Singh, G.; Shankar, R. Structural investigations of poly(methyl methacrylate) by two-dimensional NMR. *J. Mol. Struct.* **2004**, *703*, 69–81. [[CrossRef](#)]
85. Sun, X.-F.; Xie, Y.; Shan, S.; Li, W.; Sun, L. Chemically-crosslinked xylan/graphene oxide composite hydrogel for copper ions removal. *J. Polym. Environ.* **2022**; *in press*. [[CrossRef](#)]
86. Gan, Z.; Sun, X.F.; Ye, Q.; Li, Y.J.; Zhang, L.; Liu, B.C. The preparation and electrospinning of hemicellulose-grafted-poly (acrylic acid). *New Chem. Mater.* **2013**, *41*, 158–160+183. (In Chinese)
87. Gulino, A.; Condorelli, G.G.; Mineo, P.; Fragalà, I. An x-ray photoelectron spectra and atomic force microscopy characterization of silica substrates engineered with a covalently assembled siloxane monolayer. *Nanotechnology* **2005**, *16*, 2170–2175. [[CrossRef](#)] [[PubMed](#)]
88. Contino, A.; Maccarrone, G.; Fragalà, M.E.; Spitaleri, L.; Gulino, A. Conjugated gold-porphyrin monolayers assembled on inorganic surfaces. *Chem.-Eur. J.* **2017**, *23*, 14937–14943. [[CrossRef](#)] [[PubMed](#)]